OPTICS

Mechanical decoupling of quantum emitters in hexagonal boron nitride from low-energy phonon modes

Michael Hoese[1], Prithvi Reddy[2], Andreas Dietrich[1], Michael K. Koch[1], Konstantin G. Fehler[1,3], Marcus W. Doherty[2], Alexander Kubanek[1,3]*

Quantum emitters in hexagonal boron nitride were recently reported to hold unusual narrow homogeneous linewidths of tens of megahertz within the Fourier transform limit at room temperature. This unique observation was traced back to decoupling from in-plane phonon modes. Here, we investigate the origins for the mechanical decoupling. New sample preparation improved spectral diffusion, which allowed us to reveal a gap in the electron-phonon spectral density for low phonon frequencies. This sign for mechanical decoupling persists up to room temperature and explains the observed narrow lines at 300 kelvin. We investigate the dipole emission directionality and reveal preferred photon emission through channels between the layers supporting the claim for out-of-plane distorted defect centers. Our work provides insights into the underlying physics for the persistence of Fourier transform limit lines up to room temperature and gives a guide to the community on how to identify the exotic emitters.

INTRODUCTION

Fourier transform–limited (FTL) transitions in atomic systems are among the most crucial ingredients for many quantum optics experiments (*1*–*8*). Furthermore, they might become key building blocks for future large-scale quantum networks (*9*–*11*). Until recently, the systems exhibiting these transitions, where the spectral width is solely determined by the excited state lifetime, can be divided in two categories: first, atomic systems such as neutral atoms (*12*–*14*) or ions (*15*–*17*) that operate at room temperature but with a large technical overhead and with limited rates and, second, atom-like solid-state systems that can be operated in compact setups and at high rates but with the requirement for cryogenic temperatures to suppress electron-phonon interaction with the solid-state environment (*5*, *8*, *18*–*23*).

In the past few years, a new atom-like system has emerged, namely, defect centers in hexagonal boron nitrite (hBN) (*24*, *25*). The emitter evidence extraordinary optical (*23*, *26*–*31*) and spin (*32*–*34*) properties. In addition, first steps toward integrating quantum emitters in hBN into photonic devices were successfully tested (*35*–*38*). A very unique and remarkable feature is the persistence of FTL lines up to room temperature (*39*). The unusual persistence of the optical transition against interaction with its solid-state environment was traced back to decoupling from in-plane phonon modes under resonant excitation. However, besides the introduction of a consistent model, experimental proof for the mechanical decoupling is lacking.

In this work, we shed light on new physics based on a quantum emitter, which is trapped between two layers of the hBN host. We explain the underlying mechanism of the mechanical decoupling by a systematic spectroscopic study of the excitation and emission properties. At low temperatures, we extract the electron-phonon spectral density at low frequencies and examine the persistence of the mechanical isolation up to room temperature. We embed our observations into a consistent theoretical model. In the last section, we analyze the topology of different hBN flakes via atomic force microscopy (AFM) and confirm that all defect centers, which are mechanically decoupled, emit photons in parallel to the hBN layer orientation. The emission directionality is consistent with a dipole that is distorted out of plane. Our work not only gives valuable insights into the new physics of mechanical isolation of defect center in hBN but also provides guidelines to the community on how to identify those emitters. We therefore contribute important steps to use defect center in hBN in quantum optics applications that can be operated at room temperature.

RESULTS

Spectral properties

As illustrated in Fig. 1A, our proposed model for explaining the persistence of FTL lines up to room temperature rests upon mechanical decoupling of the optical transition from phonon modes in the hBN lattice (*39*). Emitters located between hBN layers may be the cause of this decoupling, because their orbitals are less susceptible to in-plane phonon distortions. To understand the underlying mechanism, we first measure the photoluminescence (PL) spectrum as input for a phonon sideband (PSB) decomposition model. This allowed us to extract the electron-phonon spectral density and associate its resonances to hBN phonon modes. We then, in turn, use resonant excitation of phonon resonances to investigate the coupling of the modes under resonant drive. Since our laser system (Sirah Matisse 2 DS) operates in a wavelength range limited to 618 to 671 nm, we focus on two emitters where one, emitter A (see Fig. 1B), can be excited resonantly and near resonantly to the zero-phonon line (ZPL) and the second one, emitter B (see Fig. 1C), can be excited further away (up to 56 nm) from the ZPL via the optical phonon mode. Emitter A features a ZPL at a wavelength of 651 nm. Its PL

[1]Institute for Quantum Optics, Ulm University, D-89081 Ulm, Germany. [2]Laser Physics Centre, Research School of Physics and Engineering, Australian National University, Australian Capital Territory 2601, Australia. [3]Center for Integrated Quantum Science and Technology (IQst), Ulm University, D-89081 Ulm, Germany.
*Corresponding author. Email: alexander.kubanek@uni-ulm.de

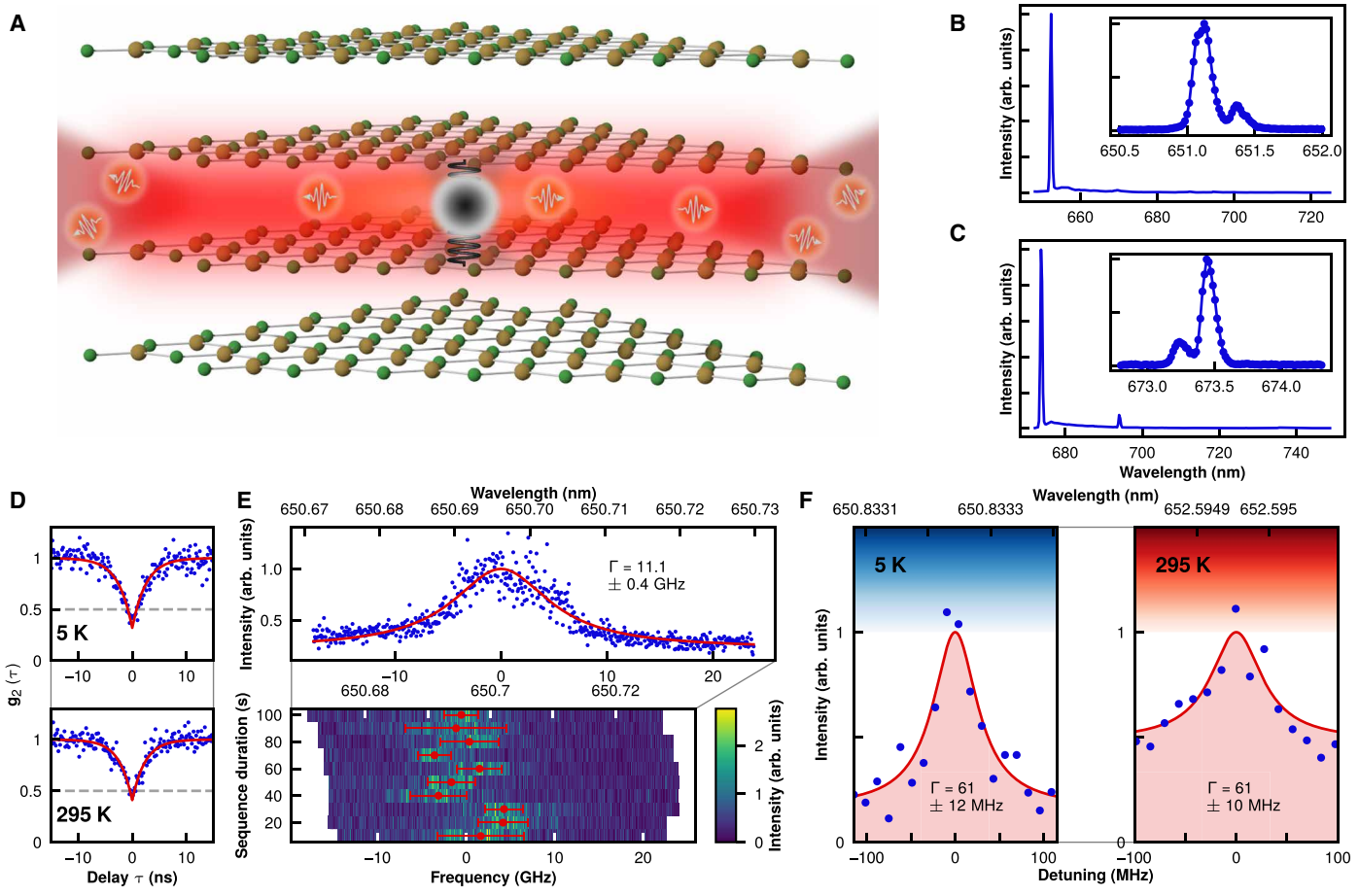

Fig. 1. Characterization and spectral properties. (**A**) Illustrative drawing of quantum emitters in hBN. (**B**) PL spectrum of emitter A. Emitter A yields an intense ZPL at 651 nm with low background. The inset shows the ZPL in high resolution, thereby revealing two distinct peaks that we identify as independent ZPLs. Since one peak is clearly dominating, the latter one can be treated as background. arb. units, arbitrary units. (**C**) PL spectrum of emitter B. The PL spectrum of emitter B is dominated by a ZPL at 673 nm. The ZPL in high resolution (see inset) shows a dominant ZPL together with a second, less intense peak compared to emitter A. (**D**) Correlation function of emitter A. The correlation function of emitter A with ZPL at 651 nm at 5 and 295 K is plotted here (blue dots), together with a fit to the data (red curve), revealing single quantum emitter characteristics with a dip at 0-ns delay below 0.5 at both temperatures. The gray lines mark the threshold at 0.5 for single-photon emitters. (**E**) Inhomogeneous linewidth of emitter A. Here, we illustrate 10 subsequent scans over the ZPL resonance. The total inhomogeneous linewidth with a Lorentzian fit to the data is shown in the top panel. Below, we plot the single scans in color scale. The red dots and error bars denote the line positions and linewidths resulting from Lorentzian fits, respectively. (**F**) Lifetime limited homogeneous lines at 5 K and room temperature. Scanning the excitation laser wavelength over the ZPL resonance reveals lifetime limited linewidths when fitting a Lorentzian (red curve) to the measurement data (blue dots) at both, cryogenic temperatures (left) and room temperature (right).

spectrum shows a low background fluorescence and high signal intensity. We measure the second-order autocorrelation function in Hanbury Brown and Twiss configuration to verify the single-photon character of our emitters. The thereby arising relatively high value of $g_2(0) = 0.32 \pm 0.03$ (see Fig. 1D) originates from a second, uncorrelated ZPL, as reported previously in (*40*). At room temperature, this value rises to $g_2(0) = 0.41 \pm 0.02$ due to higher background fluorescence. As observed in the PL spectrum at 5 K, the latter ZPL is only 0.25 nm detuned and five times less intense than the main ZPL (see Fig. 1B). Nevertheless, the single-photon character is clearly proven for 5 and 295 K, since $g_2(0) < 0.5$. Fitting the second-order correlation function

$$g_2(\tau) = 1 - a \exp\left(\frac{|\tau|}{\tau_0}\right) \quad (1)$$

to data from a correlation measurement yields a natural linewidth of 62.9 ± 3.1 MHz at cryogenic and 66.8 ± 4.2 MHz at room temperature, in line with previous reports (*29*, *41*, *42*). The excitation power is kept well below saturation to avoid power broadening. For further analysis, note that the contribution of the second emitter to the PSB emission is small. Next, we perform resonant PL excitation (PLE) spectroscopy by scanning the laser frequency over the emitter transition frequency with a tunable dye laser. The Lorentzian fit to the resonance, as illustrated in Fig. 1E, yields an inhomogeneous linewidth at 5 K of 11 ± 0.4 GHz hinting to residual spectral diffusion. Compared to earlier works (*39*), we iteratively improved our sample preparation process, resulting in clean emitter spectra and low background fluorescence. Furthermore, the cleaner substrate with less surface disturbances reduces spectral broadening and stabilizes

the emitter. Thus, we could improve the inhomogeneous linewidth by a factor of 70 at comparable excitation powers of few microwatts. For individual scans, we encounter a homogeneous linewidth within the FTL of 62.9 ± 3.1 MHz. An exemplary scan at cryogenic temperature (5 K) reveals a homogeneous linewidth of 61 ± 12 MHz, as shown in Fig. 1F. At room temperature (293 K), a scan with a measured linewidth of 61 ± 10 MHz (see Fig. 1F) confirms the FTL of the homogeneous linewidth.

PSB decomposition

Now, we study the PL spectrum of emitter A in detail to identify the defect's electron-phonon coupling mechanisms. In Fig. 2A, the blue curve shows the defect's bright ZPL emission. The grey shaded intensity shows a magnified view of the PSB, which highlights the phonon features. We applied a PSB decomposition method that adopts a linear symmetric mode model (*43*–*45*) to describe the PSB in terms of defect's electron-phonon spectral density, also referred to as the one-phonon band. The one-phonon band represents all defect processes involving the creation and/or annihilation of a single phonon. Using our method, we accurately decomposed the PSB into its one-phonon band. Further details of the decomposition process are included in the Supplementary Materials. Since the band can be accurately modeled in terms of its one-phonon band, we can assume the absence of strong vibronic interactions that involve nonsymmetric modes or introduce anharmonic effects, such as Jahn-Teller.

Next, we compare the intensities of the one-phonon band features to the intrinsic phonon modes of hBN to identify the defect's electron-phonon processes. Here, we are assuming that the emitter does not substantially perturb the modes of pristine hBN. Features in the one-phonon band correspond to frequencies of high mode density and/or where there is strong coupling to the defect orbitals. The one-phonon band is plotted against the phonon band structure of pristine hBN, as shown in Fig. 2B. The modes that couple to the defect are highlighted in green. The one-phonon band's largest feature is a broad peak centered at 11 meV. The prominence of this feature indicates that, at this frequency, two things are occurring: a high density of modes and a strong coupling to the defect. The feature is coincident with the leveling out of the B_{1g} and A_{2u} bands at the *A*-point. These are acoustic modes in the out-of-plane direction, and their qualitative atomic displacements are shown in Fig. 2C. The *A*-point corresponds to out-of-plane wave vector at the edge of the Brillouin zone. This means that *A*-point phonons also result in maximum displacement between equivalent atoms in neighboring unit cells in the interplane direction. There is a sharp feature at 50 meV that does not coincide with any critical points in the band structure, indicating that it is a local mode.

The next green highlighted peak corresponds to coupling to the A_{2u} and/or B_{1g} out-of-plane optical modes at the Γ-point, shown in Fig. 2D. The B_{1g} mode is where atoms within a layer of the unit cell move out of phase with each other, and each atom moves in phase with its nearest neighbor in the other layer. The A_{2u} mode is where each atom moves out of phase with both its in-plane and out-of-plane nearest neighbors within the unit cell. Notably, the A_{2u} mode causes relative displacement (compression/dilation) between layers. This is similar to the interplane displacements caused by the modes that coincide with the large feature at 11 meV discussed earlier. The feature at 115 meV does not coincide with any band structure detail, since it stems from the Raman line of chromium defects in the sapphire substrate and not from the emitter itself.

The remaining features of the one-phonon band imply that the defect weakly couples to the following: (i) the longitudinal acoustic E_{1u} mode at the *K*-point, (ii) potentially multiple transverse modes, and (iii) the longitudinal optical E_{1u} mode at the Γ-point. These modes correspond to in-plane displacements between neighboring unit cells of hBN. The microscopic displacements that can be associated with the last three features are quite complicated. As a result, it is not immediately obvious how they may interact with the defect. Nevertheless, these observations may still provide some insight as we develop our understanding of the defect.

The major feature of the PSB—the large peak at about 11 meV—is reproduced with two other emitters. The spectra for these emitters and their mode decomposition are presented in the Supplementary Materials. Notably, some of the higher energy features are not visible in all spectra. In particular, the local mode and the peaks at 100 and 130 meV are absent, as discussed further in the Supplementary Materials.

Given the defect's strong coupling to modes that result in out-of-plane displacements, we conclude that the orbitals of the defect exist between the layers of hBN. This is consistent with the picture presented in (*39*) that an out-of-plane distortion has led to decoupling from in-plane phonons. We generalize the result to other interplane defects similar to a trapped atom near an impurity or vacancy.

The polarization-dependent PL spectrum shown in Fig. 2 (E and F) exhibits the polarization of the full PSB. Light emitted from the ZPL shows a distinct polarization contrast. Thereto, the polarization contrast for the off-resonant excitation at 532 nm is rotated by 41° (see Fig. 2G), as observed previously (*46*), and hinting toward an additional excited state. The polarization of both the optical phonon mode at 710 nm and the low-energy acoustic phonon modes is aligned to the ZPL emission. We conclude that the involvement of phonons in the emission process does not alter the polarization contrast. This is consistent with the defect coupling to linear symmetric modes.

Coupling to excited state PSB

Next, we probe the electron-phonon coupling strength of individual phonon resonances. For this purpose, we use wavelength-dependent PLE spectroscopy. We operate the experiment in two different modes. First, we integrate the spectrum over the optical PSB from 705 to 800 nm, as illustrated in Fig. 3A, to detect the fluorescence when exciting close to the ZPL. Second, we use the integral of a Gaussian fit to the ZPL as intensity measure when exciting further away from the ZPL. Thereby, we can measure the excitation strength over a large frequency range and compare it to the PL signal when adjusting the scaling of the emitter intensity. The first observation is that we can clearly excite the first phonon feature, which can be associated with the first ZA (out-of-plane acoustic) mode, 8 meV detuned from the ZPL. The polarization contrast of the excitation on resonance with the acoustic mode yields the polarization dependence, as depicted in Fig. 3B. In contrast to the polarization of the off-resonant excitation at 532 nm, we now observe the excitation polarization aligned to the ZPL emission polarization. We conclude that we are now addressing the same excited state with a ZA phonon–assisted excitation that preserves the polarization. Figure 3C unfolds the polarization- and wavelength-dependent electron-phonon coupling across the complete phonon spectrum. We note that there is also a weak excitation probability on resonance with the ZA mode but with perpendicular polarization with respect to the ZPL emission. We interpret this observation

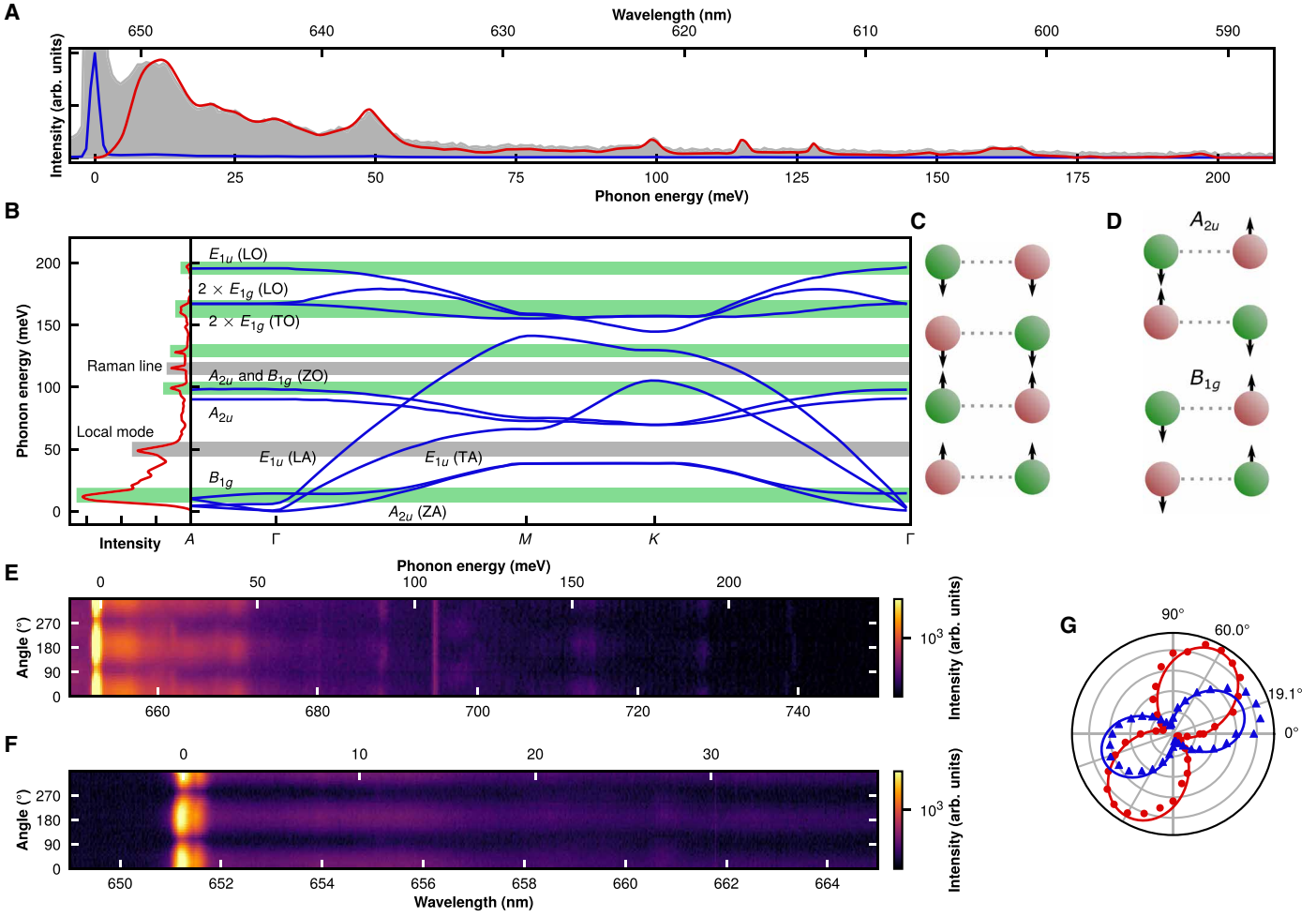

Fig. 2. Polarization-dependent PL and phonon mode decomposition. (**A**) PL spectrum. Here, we display the full spectrum (blue curve) of emitter A. For better visibility, the gray background illustrates the magnified PSB. For comparison, we plot the one-phonon band, derived from PSB decomposition in red. (**B**) Comparison of the one-phonon band and the phonon band structure. Each band in the band structure is labeled by its symmetry at the Γ-point (*48*). The green highlighted peaks in the one-phonon band (plotted in red at the left) are coincident with bands leveling off at high symmetry points in the band structure. The gray bars indicate peaks that are not coincident with any features in the band structure. The phonon mode marks label L as in-plane longitudinal, T as in-plane transverse and Z as out-of-plane combined with A for acoustic or O for optical. (**C**) The B_{1g}/A_{2u} modes at the *A*-point. Here, we illustrate the atom motion resulting in the B_{1g}/A_{2u} bands at the *A*-point. (**D**) The A_{2u} (top) and B_{1g} (bottom) modes at the Γ-point. This out-of-plane mode is sketched here with arrows denoting atom motion. (**E**) Polarization-dependent PL. The image shows a polarization-dependent PL spectroscopy with the logarithmic color scale at the ZPL at 651 nm being cut off for better total visibility. (**F**) Polarization-dependent PL in high resolution. Here, we plot polarization-dependent PL of the PSB close to the ZPL with high-resolution spectra. For better visibility, the color scale is logarithmic. (**G**) Absorption and emission polarization (532 nm). The red data points, together with the red fit, denote the polarization of the 532-nm laser light absorbed for PL spectroscopy. The polarization of light emitted from the emitter is plotted with blue dots and a blue curve marking the measurement data and the fit, respectively. Both measurements reveal a clearly distinct orientation of the 532-nm absorption and the emission dipole.

as residual excitation of the second, much weaker ZPL. Since the second ZPL of both defects is detuned by around 0.8 meV (see insets in Fig. 1, B and C), we do not resolve the splitting here. Now, we want to investigate the low-frequency gap between the ZPL and the acoustic phonon branches and therefore focus on the data polarized parallel to the ZPL emission. The fluorescence intensity and therefore the electron-phonon coupling strength display a clear minimum at about 5 meV detuned from the ZPL, confirming our findings in PL spectroscopy. The maximum on resonance with the first acoustic phonon energy at around 8 meV detuned from the ZPL resonance at 0 meV also agrees with the results from the PL spectrum. The left panel in Fig. 3C illustrates the gap width for both, PL and PLE, data. Therefore, we determine the peak positions of ZPL and PSB, respectively, and define the gap size as their difference. The figure illustrates the consistency of the gap width between PL and PLE measurement.

We now finalize our study of the electron-phonon coupling strength by investigating the optical phonon mode. Because of electromagnetic coupling between the optical transition and the optical mode, we expect electron-phonon coupling even for an emitter that is displaced out of plane of the hBN layer. Because of the limited tuning range of our laser system, we use a second emitter B with a ZPL at 673 nm to probe excitation via the optical phonon mode. The PL spectrum and the wavelength-dependent excitation are shown in Fig. 3D. The emitter can be excited efficiently via the optical phonon mode showing a distinct resonance at 165 meV

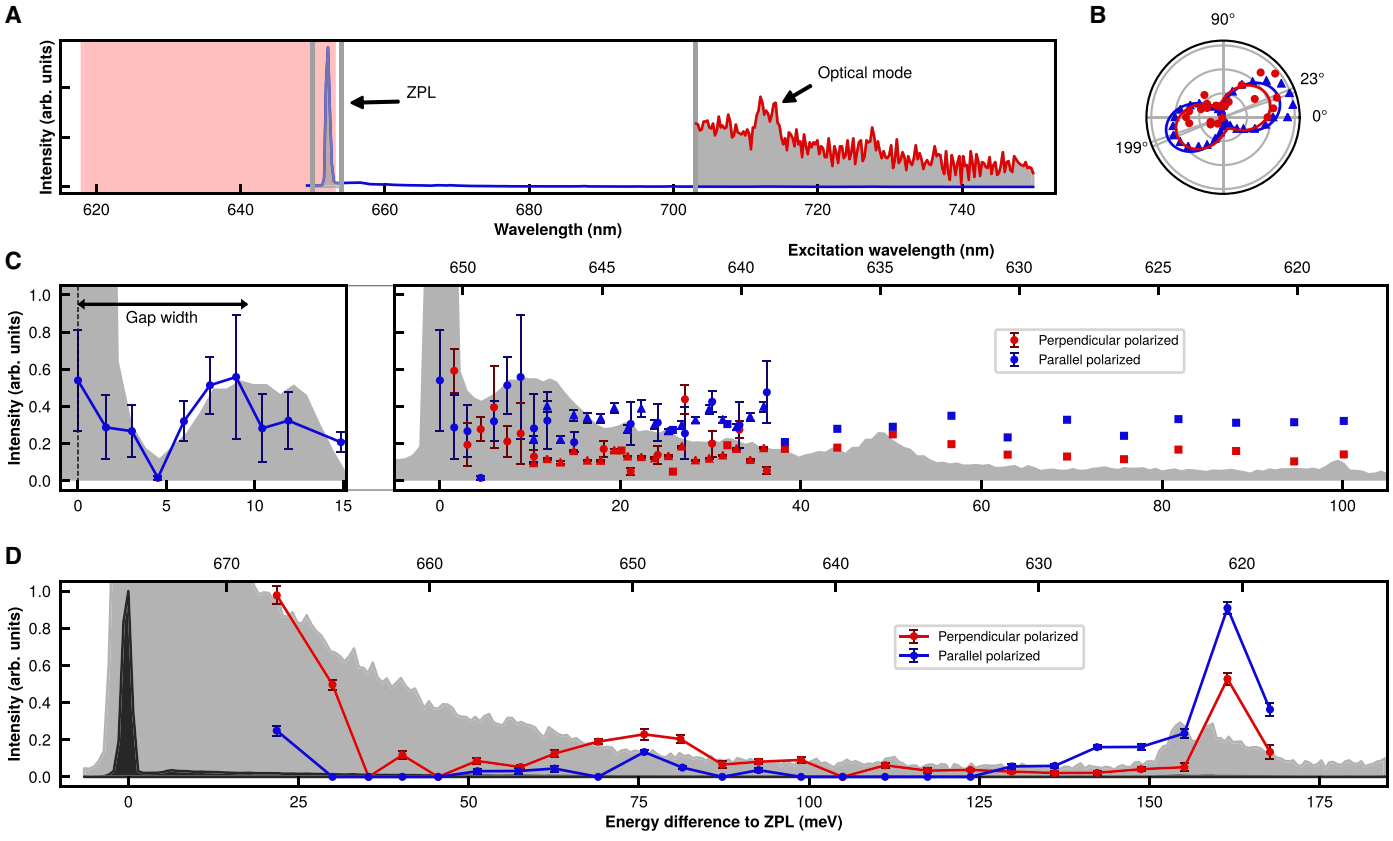

Fig. 3. Coupling to excited state PSB. (**A**) PLE measurement scheme for excitation via PSB. The blue curve shows the spectrum of emitter A, with the magnified PSB in red. The PLE excitation wavelengths are shaded in red. For detection, we integrate over ZPL or PSB as intensity measure (gray shaded areas). (**B**) Polarization of first phonon mode. We excite emitter A 6.8 meV detuned from resonance. We fit the results with a sine (red), yielding a polarization angle of 23°. For comparison, we plot the ZPL emission polarization in blue. (**C**) Polarization-dependent PLE at the excitation PSB. In the right panel, blue and red dots represent results for excitation with parallel and perpendicular polarized light. Circles and triangles denote two different measurement runs, using the optical mode for detection. Squares extend the measurement to higher energy differences with data extracted from the ZPL integral. The gray shaded spectrum is a mirrored PL spectrum for comparison. In the left panel, we illustrate the extracted gap width with rescaled intensity. (**D**) PLE at the excitation PSB with emitter B. We plot results extracted from the ZPL integral for parallel (blue) and perpendicular polarization (red). The dark gray shaded curve is the PL spectrum mirrored at the ZPL. The magnified PSB is plotted in lighter gray.

detuned from the ZPL and in agreement with previous results (*47*). The polarization of the excitation laser is again aligned with the polarization of the ZPL emission, confirming that the phonon-assisted excitation does not alter the polarization properties. Please also note that, in this case, we do observe a second ZPL with an intensity of approximately half of the first ZPL. That ZPL could explain the residual excitation probability perpendicular to the ZPL emission. Furthermore, please note that we observe signs of additional modes in excitation at a detuning of approximately 75 meV from the ZPL. However, assigning these resonances to modes in the PL spectrum is not distinct.

Temperature-dependent gap size

In the following, we focus on the temperature dependence of the gap in the electron-phonon spectral density and its persistence up to room temperature. We extrapolate the gap size by fitting a Gaussian to the ZPL and to the first acoustic phonon feature and determine the gap size as distance between both peaks. An example is illustrated in Fig. 4A. A characterization of 33 different emitters yields an average gap size of about 2 THz within a distribution of approximately 1 THz, as illustrated in Fig. 4B. The histogram is asymmetric and drops faster toward smaller gap size, since smaller gap widths are more difficult to resolve. To be able to observe the gap, its size needs to be larger than the ZPL linewidth. We characterize both the gap size of emitters A and B for different temperatures from 5 to 300 K, as plotted in Fig. 4 (C and D), respectively, and plot it against the ZPL linewidth. With rising temperature, the gap size narrows, whereas the width of the ZPL increases. The gap of both emitters remains open and observable all the way to room temperature. However, the gap size at 300 K decreases to about half the size at 5 K, while the ZPL width increases to almost half the gap size at 300 K. We fit the temperature dependence of both, the ZPL linewidth and the gap size, with the Boltzmann function

$$w = A + B \cdot \exp\left(-\frac{C}{k_B T}\right) \quad (2)$$

with w denoting the gap size or the ZPL width and the fit constants A, B, and C and extrapolate a gap size of 1.14 ± 0.24 THz at 294.2 K with a ratio for the Boltzmann energy of $\frac{hf}{k_B T} = 0.186 \pm 0.039$. This dependence could arise from a temperature-dependent distortion that modifies the electron-phonon couplings and phonon frequencies. For example, this could be a further out-of-plane distortion of

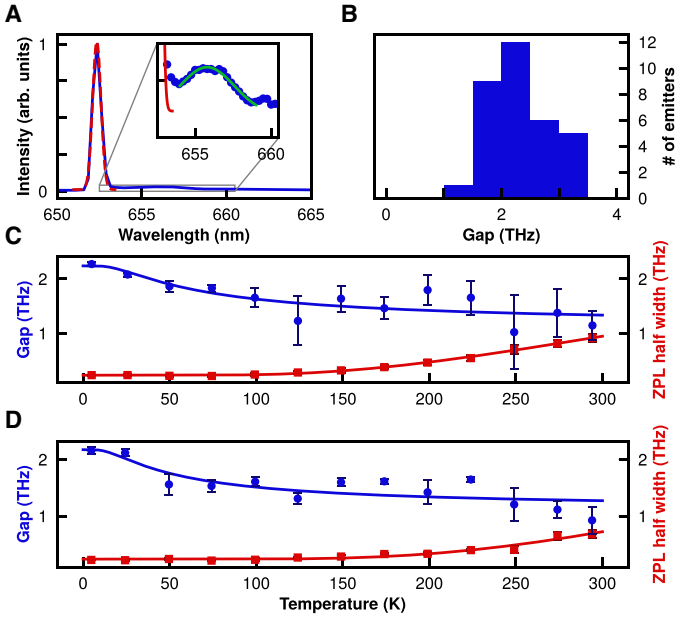

Fig. 4. Temperature-dependent gap size. (**A**) Gap size analysis procedure. For evaluation of the gap size, we fit a Gaussian (dashed red curve) to the ZPL in the PL spectrum (blue curve) and to the PSB. The inset shows the fitted PSB (green curve) with the PL spectrum (blue dots). (**B**) Gap size distribution. We determine the gap size of multiple emitters at 5 K and display the abundance distribution, peaking at 2 THz. (**C**) Evolution of the gap size. Here, we measured the gap size (blue points) and the half width of the ZPL (red squares) for different temperatures. The data here stem from emitter A, which we used for resonant PLE and PLE at the excitation PSB. For extrapolation, we assumed proportionality of both measurement values to the Boltzmann factor. The fitted curves are plotted in blue and red for the according parameters, respectively. (**D**) Evolution of the gap size. As in (C), we depict the gap data for emitter B using the same labeling.

an already distorted defect or changes to the configuration of an interplane defect. For changes in the electron-phonon coupling to shift the energies of PSB features, there must be a difference in the phonon frequencies between the two electronic levels of the optical transition. This is a higher-order effect that is not captured by the linear symmetric mode model and warrants future investigation.

AFM flake characterization

Last, we characterize the topology of the hBN flakes with an atomic force microscope. We compare the flake texture between flakes hosting emitters with and without gap in the electron-phonon density of states. The AFM scan of the height profile reveals the angle of the hBN flake surface with respect to the substrate surface, which we equalize to the hBN layer orientation. Two exemplary scans are shown in Fig. 5. We now gain insights into the mechanical decoupling mechanism by correlating the tilt angle of the hBN flakes hosting the defect centers with the gap size observed in the PL spectrum. If an out-of-plane distortion of the emitter is the origin for the mechanical decoupling, then all emitters with a gap should only be observable in tilted hBN flakes. In contrast, all emitters without a gap should predominantly be observed in hBN flakes lying flat on the surface corresponding to small tilt angles. This correlation is clearly visible in Fig. 5. In total, 45 emitters are studied. All emitters with no gap in the PL spectrum are observed in hBN flakes with a tilt angle below 50°. Every second flake has a tilt of less than 12°. Vice versa, all flakes hosting emitters with a gap in the PL spectrum yield tilt of at least 12°. Possibly, the dipole of emitters with gap is distorted out of plane, and the emission tends to spread along the hBN layers. This results in a better visibility when the flake is tilted such that the hBN layers and the emitted light points toward the objective for collection. On the other hand, in-plane defects result in gapless emitters. Since their dipoles are also located in-plane, the emission is mostly perpendicular to the hBN layers. We observe this class of emitters in flakes with small tilt angles.

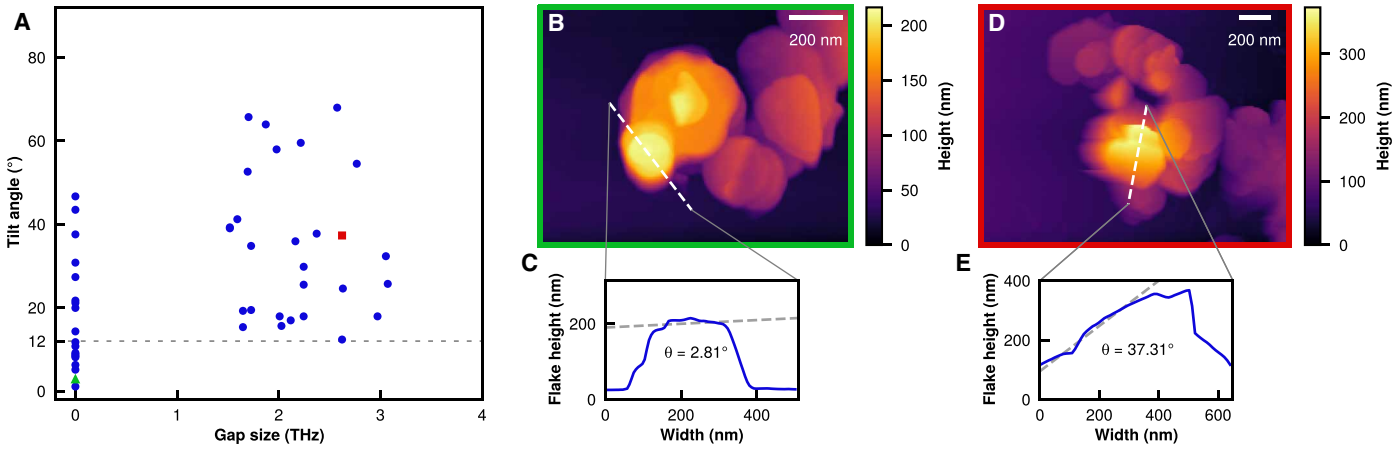

Fig. 5. AFM characterization. Here, we present the key results of an AFM characterization of flakes hosting quantum emitters with and without gap between ZPL and PSB. The left plot (**A**) depicts the tilt angle of host flakes versus the gap size of the emitters. The dashed black line marks 12° tilt, thereby highlighting the minimum tilt for emitters with gap. In (**B**), we illustrate the flake that provides the data of the green triangle in (A). The white dashed line in the three-dimensional (3D) AFM height profile marks the segment we use for measuring the tilt of the flake. Below, we plot this 2D height profile (**C**), together with a straight dashed line illustrating the tilt angle determination. In the same manner, we exemplary picture one flake hosting an emitter with gap in the right panel (**D**). The 2D height profile (**E**) reveals the strong tilt of the host flake resulting in the red squared data point in (A).

DISCUSSION

In summary, we confirm that some defect centers in hBN exhibit mechanically decoupled electronic transitions under resonant excitation. Improved sample preparation enabled a 70-fold decrease in spectral diffusion and allowed us, in this work, to observe a gap of around 2 THz in the electron-phonon density of states, which remains open up to room temperature. In a systemic study of the coupling to individual modes, we developed a model where the emitter has orbitals that exist between the layers of hBN. This model was proposed in (*39*) to explain the persistence of FTL linewidths in resonant excitation up to room temperature. We furthermore categorize common features of all emitters with decoupled optical transitions showing a gap in the PL- and wavelength-dependent PLE spectrum between ZPL and first acoustic phonon modes. Our results imply that only multilayer hBN flakes can serve as host for this emitter type. Furthermore, the emission directionality is shifted toward an emission parallel to the hBN layer. Besides new insights into the physics explaining the extraordinary observation of FTL lines at room temperature, our work also outlines a catalog that could be used in future experiments to identify mechanically decoupled emitters. Our work therefore opens up new ways to use defect center in hBN for quantum optics applications at room temperature.

METHODS

We perform all measurements with a sample made of commercially available monolayer hBN flakes (2D Semiconductors), spin-coated onto a sapphire substrate. Afterwards, we anneal the sample at 800°C for 30 min. For all optical measurements, the sample is mounted in a flow cryostat with a standard confocal microscope setup. We can cool the sample to 5 K with liquid helium and heat it to warmer temperatures up to room temperature for temperature-dependent measurements. For excitation, we have a 532-nm diode laser (Laser Quantum gem 532) for PL measurements and a tunable (618 to 671 nm) dye laser (Sirah Matisse 2 DS) for PLE measurements at hand. We detect signals with two avalanche photo diodes (PicoQuant) and a spectrometer (Princeton Instruments). By scanning the tunable dye laser over the resonance, we measure the homogeneous linewidth. PLE via the PSB of the excited state is measured by setting the excitation laser to a certain wavelength and acquiring a spectrum. Depending on the excitation wavelength and our ability to separate excitation laser and signal with optical filters, we either use the optical PSB or the ZPL for detection. For polarization control, we use an achromatic half–wave plate in the excitation path. AFM measurements are performed with a separate AFM (Bruker JPK). Therefore, we remove the sample from the cryostat and place it under the AFM.

For PSB decomposition, we start with an unprocessed PL spectrum of the emitter. Then, we apply multiple preprocessing steps described in the Supplementary Materials to extract the one-phonon band.

SUPPLEMENTARY MATERIALS

Supplementary material for this article is available at http://advances.sciencemag.org/cgi/content/full/6/40/eaba6038/DC1

REFERENCES AND NOTES

1. T. Legero, T. Wilk, M. Hennrich, G. Rempe, A. Kuhn, Quantum beat of two single photons. *Phys. Rev. Lett.* **93**, 070503 (2004).
2. D. L. Moehring, P. Maunz, S. Olmschenk, K. C. Younge, D. N. Matsukevich, L. M. Duan, C. Monroe, Entanglement of single-atom quantum bits at a distance. *Nature* **449**, 68–71 (2007).
3. R. Lettow, Y. L. A. Rezus, A. Renn, G. Zumofen, E. Ikonen, S. Götzinger, V. Sandoghdar, Quantum interference of tunably indistinguishable photons from remote organic molecules. *Phys. Rev. Lett.* **104**, 123605 (2010).
4. E. Togan, Y. Chu, A. S. Trifonov, L. Jiang, J. Maze, L. Childress, M. V. G. Dutt, A. S. Sørensen, P. R. Hemmer, A. S. Zibrov, M. D. Lukin, Quantum entanglement between an optical photon and a solid-state spin qubit. *Nature* **466**, 730–734 (2010).
5. A. Sipahigil, M. L. Goldman, E. Togan, Y. Chu, M. Markham, D. J. Twitchen, A. S. Zibrov, A. Kubanek, M. D. Lukin, Quantum interference of single photons from remote nitrogen-vacancy centers in diamond. *Phys. Rev. Lett.* **108**, 143601 (2012).
6. S. Ritter, C. Nölleke, C. Hahn, A. Reiserer, A. Neuzner, M. Uphoff, M. Mücke, E. Figueroa, J. Bochmann, G. Rempe, An elementary quantum network of single atoms in optical cavities. *Nature* **484**, 195–200 (2012).
7. H. Bernien, B. Hensen, W. Pfaff, G. Koolstra, M. Blok, L. Robledo, T. Taminiau, M. Markham, D. Twitchen, L. Childress, R. Hanson, Heralded entanglement between solid-state qubits separated by three metres. *Nature* **497**, 86–90 (2013).
8. A. Sipahigil, K. D. Jahnke, L. J. Rogers, T. Teraji, J. Isoya, A. S. Zibrov, F. Jelezko, M. D. Lukin, Indistinguishable photons from separated silicon-vacancy centers in diamond. *Phys. Rev. Lett.* **113**, 113602 (2014).
9. H. Kimble, The quantum internet. *Nature* **453**, 1023–1030 (2008).
10. A. Sipahigil, R. E. Evans, D. D. Sukachev, M. J. Burek, J. Borregaard, M. K. Bhaskar, C. T. Nguyen, J. L. Pacheco, H. A. Atikian, C. Meuwly, R. M. Camacho, F. Jelezko, E. Bielejec, H. Park, M. Lončar, M. D. Lukin, An integrated diamond nanophotonics platform for quantum-optical networks. *Science* **354**, 847–850 (2016).
11. S. Wehner, D. Elkouss, R. Hanson, Quantum internet: A vision for the road ahead. *Science* **362**, eaam9288 (2018).
12. A. Kuhn, M. Hennrich, G. Rempe, Deterministic single-photon source for distributed quantum networking. *Phys. Rev. Lett.* **89**, 067901 (2002).
13. B. Darquié, M. P. A. Jones, J. Dingjan, J. Beugnon, S. Bergamini, Y. Sortais, G. Messin, A. Browaeys, P. Grangier, Controlled single-photon emission from a single trapped two-level atom. *Science* **309**, 454–456 (2005).
14. J. K. Thompson, J. Simon, H. Loh, V. Vuletić, A high-brightness source of narrowband, identical-photon pairs. *Science* **313**, 74–77 (2006).
15. P. Maunz, D. L. Moehring, S. Olmschenk, K. C. Younge, D. N. Matsukevich, C. Monroe, Quantum interference of photon pairs from two remote trapped atomic ions. *Nat. Phys.* **3**, 538–541 (2007).
16. H. G. Barros, A. Stute, T. E. Northup, C. Russo, P. O. Schmidt, R. Blatt, Deterministic single-photon source from a single ion. *New J. Phys.* **11**, 103004 (2009).
17. M. Almendros, J. Huwer, N. Piro, F. Rohde, C. Schuck, M. Hennrich, F. Dubin, J. Eschner, Bandwidth-tunable single-photon source in an ion-trap quantum network. *Phys. Rev. Lett.* **103**, 213601 (2009).
18. L. Sapienza, M. Davanço, A. Badolato, K. Srinivasan, Nanoscale optical positioning of single quantum dots for bright and pure single-photon emission. *Nat. Commun.* **6**, 7833 (2015).
19. A. V. Kuhlmann, J. H. Prechtel, J. Houel, A. Ludwig, D. Reuter, A. D. Wieck, R. J. Warburton, Transform-limited single photons from a single quantum dot. *Nat. Commun.* **6**, 8204 (2015).
20. J.-P. Jahn, M. Munsch, L. Béguin, A. V. Kuhlmann, M. Renggli, Y. Huo, F. Ding, R. Trotta, M. Reindl, O. G. Schmidt, A. Rastelli, P. Treutlein, R. J. Warburton, An artificial rb atom in a semiconductor with lifetime-limited linewidth. *Phys. Rev. B* **92**, 245439 (2015).
21. X.-L. Chu, S. Götzinger, V. Sandoghdar, A single molecule as a high-fidelity photon gun for producing intensity-squeezed light. *Nat. Photonics* **11**, 58–62 (2017).
22. M. K. Bhaskar, D. D. Sukachev, A. Sipahigil, R. E. Evans, M. J. Burek, C. T. Nguyen, L. J. Rogers, P. Siyushev, M. H. Metsch, H. Park, F. Jelezko, M. Lončar, M. D. Lukin, Quantum nonlinear optics with a germanium-vacancy color center in a nanoscale diamond waveguide. *Phys. Rev. Lett.* **118**, 223603 (2017).
23. A. Dietrich, M. Bürk, E. S. Steiger, L. Antoniuk, T. T. Tran, M. Nguyen, I. Aharonovich, F. Jelezko, A. Kubanek, Observation of fourier transform limited lines in hexagonal boron nitride. *Phys. Rev. B* **98**, 081414 (2018).
24. T. T. Tran, K. Bray, M. J. Ford, M. Toth, I. Aharonovich, Quantum emission from hexagonal boron nitride monolayers. *Nat. Nanotechnol.* **11**, 37–41 (2016).
25. M. Toth, I. Aharonovich, Single photon sources in atomically thin materials. *Annu. Rev. Phys. Chem.* **70**, 123–142 (2019).
26. G. Grosso, H. Moon, B. Lienhard, S. Ali, D. K. Efetov, M. M. Furchi, P. Jarillo-Herrero, M. J. Ford, I. Aharonovich, D. Englund, Tunable and high-purity room temperature single-photon emission from atomic defects in hexagonal boron nitride. *Nat. Commun.* **8**, 705 (2017).
27. G. Noh, D. Choi, J.-H. Kim, D.-G. Im, Y.-H. Kim, H. Seo, J. Lee, Stark tuning of single-photon emitters in hexagonal boron nitride. *Nano Lett.* **18**, 4710–4715 (2018).
28. N. V. Proscia, Z. Shotan, H. Jayakumar, P. Reddy, C. Cohen, M. Dollar, A. Alkauskas, M. Doherty, C. A. Meriles, V. M. Menon, Near-deterministic activation of room-temperature quantum emitters in hexagonal boron nitride. *Optica* **5**, 1128–1134 (2018).

29. T. T. Tran, M. Kianinia, M. Nguyen, S. Kim, Z.-Q. Xu, A. Kubanek, M. Toth, I. Aharonovich, Resonant excitation of quantum emitters in hexagonal boron nitride. *ACS Photonics* **5**, 295–300 (2018).
30. K. Konthasinghe, C. Chakraborty, N. Mathur, L. Qiu, A. Mukherjee, G. D. Fuchs, A. N. Vamivakas, Rabi oscillations and resonance fluorescence from a single hexagonal boron nitride quantum emitter. *Optica* **6**, 542–548 (2019).
31. N. Nikolay, N. Mendelson, E. Özelci, B. Sontheimer, F. Böhm, G. Kewes, M. Toth, I. Aharonovich, O. Benson, Direct measurement of quantum efficiency of single-photon emitters in hexagonal boron nitride. *Optica* **6**, 1084–1088 (2019).
32. A. L. Exarhos, D. A. Hopper, R. N. Patel, M. W. Doherty, L. C. Bassett, Magnetic-field-dependent quantum emission in hexagonal boron nitride at room temperature. *Nat. Commun.* **10**, 222 (2019).
33. A. Gottscholl, M. Kianinia, V. Soltamov, S. Orlinskii, G. Mamin, C. Bradac, C. Kasper, K. Krambrock, A. Sperlich, M. Toth, I. Aharonovich, V. Dyakonov, Initialization and read-out of intrinsic spin defects in a van der waals crystal at room temperature. *Nat. Mater.* **19**, 540–545 (2020).
34. N. Chejanovsky, A. Mukherjee, Y. Kim, A. Denisenko, A. Finkler, T. Taniguchi, K. Watanabe, D. Bhaktavatsala Rao Dasari, J. H. Smet, J. Wrachtrup, Single spin resonance in a van der Waals embedded paramagnetic defect. arXiv:1906.05903 [cond-mat.mes-hall] (13 June 2019).
35. A. W. Schell, H. Takashima, T. T. Tran, I. Aharonovich, S. Takeuchi, Coupling quantum emitters in 2d materials with tapered fibers. *ACS Photonics* **4**, 761–767 (2017).
36. T. T. Tran, D. Wang, Z.-Q. Xu, A. Yang, M. Toth, T. W. Odom, I. Aharonovich, Deterministic coupling of quantum emitters in 2d materials to plasmonic nanocavity arrays. *Nano Lett.* **17**, 2634–2639 (2017).
37. S. Kim, J. E. Fröch, J. Christian, M. Straw, J. Bishop, D. Totonjian, K. Watanabe, T. Taniguchi, M. Toth, I. Aharonovich, Photonic crystal cavities from hexagonal boron nitride. *Nat. Commun.* **9**, 2623 (2018).
38. T. Vogl, R. Lecamwasam, B. C. Buchler, Y. Lu, P. K. Lam, Compact cavity-enhanced single-photon generation with hexagonal boron nitride. *ACS Photonics* **6**, 1955–1962 (2019).
39. A. Dietrich, M. W. Doherty, I. Aharonovich, A. Kubanek, Solid-state single photon source with fourier transform limited lines at room temperature. *Phys. Rev. B* **101**, 081401 (2020).
40. A. Bommer, C. Becher, New insights into nonclassical light emission from defects in multi-layer hexagonal boron nitride. *Nanophotonics* **8**, 2041–2048 (2019).
41. T. T. Tran, C. Elbadawi, D. Totonjian, C. J. Lobo, G. Grosso, H. Moon, D. R. Englund, M. J. Ford, I. Aharonovich, M. Toth, Robust multicolor single photon emission from point defects in hexagonal boron nitride. *ACS Nano* **10**, 7331–7338 (2016).
42. B. Sontheimer, M. Braun, N. Nikolay, N. Sadzak, I. Aharonovich, O. Benson, Photodynamics of quantum emitters in hexagonal boron nitride revealed by low-temperature spectroscopy. *Phys. Rev. B* **96**, 121202 (2017).
43. G. Davies, Vibronic spectra in diamond. *J. Phys. C Solid State Phys.* **7**, 3797–3809 (1974).
44. P. Kehayias, M. W. Doherty, D. English, R. Fischer, A. Jarmola, K. Jensen, N. Leefer, P. Hemmer, N. B. Manson, D. Budker, Infrared absorption band and vibronic structure of the nitrogen-vacancy center in diamond. *Phys. Rev. B* **88**, 165202 (2013).
45. P. Balasubramanian, M. H. Metsch, P. Reddy, L. J. Rogers, N. B. Manson, M. W. Doherty, F. Jelezko, Discovery of st1 centers in natural diamond. *Nanophotonics* **8**, 1993–2002 (2019).
46. N. R. Jungwirth, B. Calderon, Y. Ji, M. G. Spencer, M. E. Flatté, G. D. Fuchs, Temperature dependence of wavelength selectable zero-phonon emission from single defects in hexagonal boron nitride. *Nano Lett.* **16**, 6052–6057 (2016).
47. D. Wigger, R. Schmidt, O. D. Pozo-Zamudio, J. A. Preuß, P. Tonndorf, R. Schneider, P. Steeger, J. Kern, Y. Khodaei, J. Sperling, S. M. de Vasconcellos, R. Bratschitsch, T. Kuhn, Phonon-assisted emission and absorption of individual color centers in hexagonal boron nitride. *2D Mater.* **6**, 035006 (2019).
48. I. Hamdi, N. Meskini, Ab initio study of the structural, elastic, vibrational and thermodynamic properties of the hexagonal boron nitride: Performance of lda and gga. *Phys. B Condens. Matter* **405**, 2785–2794 (2010).

Acknowledgments: We thank K. Gottschalk and F. Erb for support. **Funding:** The project was funded by the Deutsche Forschungsgemeinschaft (DFG; German Research Foundation)—project number: 398628099. A.K. acknowledges support of the European Regional Development Fund (EFRE) program Baden-Württemberg. M.W.D. acknowledges support from the Australian Research Council (DE170100169). K.G.F. and A.K. acknowledge support of IQst. M.H. acknowledges support from the Studienstiftung des deutschen Volkes. The AFM was funded by the DFG. **Author contributions:** M.H., A.D., and A.K. conceived the experiments. All PL and PLE measurements were performed by M.H., A.D., and M.K.K., who also analyzed the results. K.G.F., together with M.H. and M.K.K., conducted the AFM characterization. P.R. and M.W.D. performed the PSB decomposition analysis. All authors discussed the results. M.H., P.R., and A.K. wrote the manuscript, which was discussed and edited by all authors. **Competing interests:** The authors declare that they have no competing interests. **Data and materials availability:** All data needed to evaluate the conclusions in the paper are present in the paper and/or the Supplementary Materials. Readers can contact M.H. and A.K. for access to our data. Additional data related to this paper may be requested from the authors.

Submitted 20 December 2019
Accepted 14 August 2020
Published 30 September 2020
10.1126/sciadv.aba6038

Citation: M. Hoese, P. Reddy, A. Dietrich, M. K. Koch, K. G. Fehler, M. W. Doherty, A. Kubanek, Mechanical decoupling of quantum emitters in hexagonal boron nitride from low-energy phonon modes. *Sci. Adv.* **6**, eaba6038 (2020).

ScienceAdvances

Mechanical decoupling of quantum emitters in hexagonal boron nitride from low-energy phonon modes

Michael HoesePrithvi ReddyAndreas DietrichMichael K. KochKonstantin G. FehlerMarcus W. DohertyAlexander Kubanek

Sci. Adv., 6 (40), eaba6038. • DOI: 10.1126/sciadv.aba6038

Science Advances (ISSN 2375-2548) is published by the American Association for the Advancement of Science. 1200 New York Avenue NW, Washington, DC 20005. The title *Science Advances* is a registered trademark of AAAS.